

# Cavity-depth Effect on 3D Wafer-level-packaged MEMS Resonators by Slide-film Damping

Hengmao Liang,\* Shilei Lv, Songjia Han, Hongshan Liu, and Yongbing Long

College of Electronic Engineering (College of Artificial Intelligence), South China Agricultural University,  
No.483 Wushan Road, Tianhe District, Guangzhou 510642, P.R.China

(Received October 23, 2023; accepted November 13, 2023)

**Keywords:** slide-film damping, cavity depth, MEMS resonator, wafer-level packaging, damping coefficient, quality factor

The slide-film damping effect caused by cavity structures is easily neglected in the design of bulk-micro-machined resonant MEMS device fabrication and packaging processes. On the basis of theory calculations, simulations, and actual tests, in this study, we investigate the cavity-depth effect on 3D wafer-level packaged MEMS resonators with the in-plane-motion mode, in which slide-film damping is dominant. On the one hand, it is found that the slide-film damping coefficient is inversely proportional to the cavity depth and remains stable for the cavity depth above a specific value. The critical cavity depth acquired from theoretical results is  $\sim 10\ \mu\text{m}$ , which is distinct from that of  $\sim 30\ \mu\text{m}$  from simulation results. On the other hand, the variation tendency of simulation results is more in agreement with those of test results for fabricated devices than the theoretical prediction. Hence, before the structure fabrication for a resonator dominated by slide-film damping, it is imperative to choose a conservative cavity depth with a relatively high value from the combination of theory and simulation analyses, so as to ensure the high or desired  $Q$ -factors of fabricated resonators, particularly in wafer-level packaging with the low-vacuum or atmospheric pressure. Overall, this work provides not only an analysis strategy on device cavities' slide-film damping but also the optimization design of wafer-level packaging structures and processes.

## 1. Introduction

MEMS technology has been extensively used to fabricate diverse devices, given its advantages of small size, lightweight, low cost, low power consumption, high yield, and easy integration. Most MEMS sensors and actuators rely on resonators for transferring various physical and chemical quantities. However, MEMS devices usually have movable structures, which are vulnerable to external forces and environmental impacts. Therefore, packaging is essential to safeguard delicate MEMS motion structures and to enhance device performance. For example, vacuum packaging and hermetic packaging are usually implemented to improve

---

\*Corresponding author: e-mail: [lianghm@scau.edu.cn](mailto:lianghm@scau.edu.cn)  
<https://doi.org/10.18494/SAM4707>

MEMS resonators' quality factors by reducing air damping (e.g., the gyroscope) and to optimize devices' dynamic responses by adjusting air damping (e.g., the accelerometer), respectively.

Undoubtedly, analyzing air-damping characteristics, which consist of two main aspects of squeeze film damping and slide film damping, is essential for the optimized design of MEMS devices.<sup>(1)</sup> In a typical MEMS fabrication process, movable structures must be supported by fixed structures and suspended above the cavity structures in the substrate wafer. In addition, cavity structures are demanded to form in the cap wafer to provide the motion room for movable structures in a typical wafer-level packaging process of MEMS devices. These cavity structures can also introduce the air-damping effect.<sup>(2)</sup> In recent studies, cavity depth has been regarded as a notable parameter to improve MEMS device performance by optimizing cavity damping.

For instance, the performance characteristics of MEMS/NEMS pressure sensors,<sup>(3)</sup> mirrors,<sup>(4,5)</sup> microphones,<sup>(6)</sup> and accelerometers<sup>(7)</sup> are partly dependent on squeeze film damping, which is concerned with cavity depth. To avoid bouncing back, the over-damping condition of RF MEMS switches is required in device packages and thus can be realized by regulating the cap cavity depth.<sup>(8)</sup> In addition, it is identified that MEMS resonators' quality factors of packaged ones (under atmospheric pressure) are smaller than those of unpackaged ones owing to squeeze film damping from cap and substrate cavities,<sup>(9)</sup> which is similarly reported in studies on MEMS switches<sup>(10)</sup> and energy harvesters.<sup>(11,12)</sup> Also, some studies indicate that the squeeze film damping coefficient of MEMS resonators decreases with increasing cavity depth, e.g., in the MEMS rotary motors<sup>(13)</sup> and scanners.<sup>(14)</sup> The latest research puts forward that the pressures in MEMS packages can be modulated by the cavity depth because of the air-damping effect.<sup>(15,16)</sup>

Above all, the current literature mainly focuses on the impact of squeeze film damping from cavity depth selections on device performance. However, there is a lack of in-depth analysis on the slide-film damping caused by cavity depth, which is also crucial for the final performance of in-plane-motion resonant MEMS devices and their wafer-level packaging. Based on the proposed 3D wafer-level packaging technology for MEMS in our previous works,<sup>(17,18)</sup> we investigated the cavity-depth effect on the packaged MEMS resonators dominated by slide-film damping from the theory calculation, simulation, and experimental test.

## 2. Device Sketch

In this work, a type of bulk-micro-machined MEMS resonator with comb structures is adopted to discuss the slide-film damping effect of cavities. As seen in Fig. 1(a), the resonant structure is held up by four anchors at the four corners of the MEMS resonator. As the fixed framework, the comb-driving structure parts are distributed around the four sides of the resonant structure and connected through the planar interconnection of Si. Moreover, comb-detection structure parts are fixed and located inside the resonant structure. Additionally, the four long beams coupled with the eight folded beams constitute the main body of the resonant structure. Movable comb structures are only distributed on both sides of long beams. With the electrostatic driving of outer comb structures, this MEMS resonator can be excited into the in-plane contraction expansion mode with the resonant frequency of  $\sim 37.6$  kHz, as shown in Fig. 1(b).

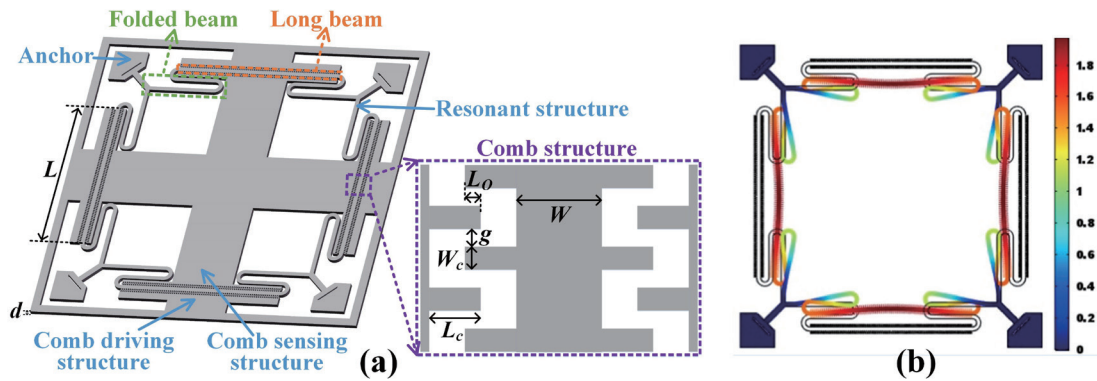


Fig. 1. (Color online) Sketch of the adopted MEMS resonator with comb structures (a) and its resonance mode (b).

With the electrostatic detection of inner comb structures, the resonance characteristics of MEMS resonators can be acquired. Table 1 presents the design values of critical structure parameters for the MEMS resonator, especially for the long beams and comb structures.

### 3. Theory Analysis and Simulation

#### 3.1 Damping theory analysis

We mainly focus on the cavity-depth effect on air damping when bulk-micro-machined MEMS resonators are bare at atmospheric pressure and wafer-level-packaged at low-vacuum pressure (even the atmospheric pressure). On such occasions, the air damping is the main source of energy dissipation. The air-damping characteristic of the MEMS resonator with combs is dominated by slide-film damping. Even though the air damping between movable and fixed comb sidewalls is primarily considered, the substrate cavity can also introduce slide-film damping. After wafer-level packaging, the substrate and cap cavities can lead to slide-film damping at the same time. According to the in-plane motion mode of MEMS resonators, slide-film damping sources include two aspects: air damping due to combs and air damping from cavities. Thus, the overall air damping coefficient  $c_{total}$  of the resonator can be expressed as Eq. (1) by the comb damping coefficient  $c_{comb}$  and the cavity damping coefficient  $c_{cavity}$ .

$$c_{total} = c_{comb} + c_{cavity} \quad (1)$$

Assuming that the movable beam resonates in a single direction, the Navier–Stokes equation suitable for slide-film damping can be simplified as a 1D equation.<sup>(19)</sup> In the slide-film damping analysis, the Couette-type flow model is feasible when the air gap is far less than the effective decay distance  $\delta$  in Eq. (2). Otherwise, the Stokes-type flow model is useful. The  $\mu_{air}$  and  $\nu_{air}$  set as  $1.8 \times 10^{-5}$  Pa·s and  $14.8 \times 10^{-6}$  m<sup>2</sup>/s are air's dynamic and kinematic viscosities, respectively. Also,  $\omega_0$  is the angular resonance frequency of resonators. Taking the resonance frequency of

Table 1.

Design values of critical structure parameters for the MEMS resonator in this work.

Device parameter	Structure thickness, $d$	Long beam length, $L$	Long beam width, $W$	Comb length, $L_c$	Comb width, $W_c$	Comb gap, $g$	Comb overlap length, $L_o$	Comb pair, $n$
Design value	50 $\mu\text{m}$	2000 $\mu\text{m}$	50 $\mu\text{m}$	30 $\mu\text{m}$	10 $\mu\text{m}$	2 $\mu\text{m}$	10 $\mu\text{m}$	332

$\sim 37.6$  kHz,  $\delta$  is calculated as  $\sim 11$   $\mu\text{m}$ . Considering that the comb gap of 2  $\mu\text{m}$  and the cavity depth above 2  $\mu\text{m}$  are not considerably smaller than the  $\delta$  value of  $\sim 11$   $\mu\text{m}$  in this work, the Stokes-type flow model <sup>(19)</sup> is adopted to obtain  $c_{comb}$  and  $c_{cavity}$  in Eqs. (3) and (4) based on Table 1.  $h_s$  and  $h_c$  are the substrate cavity and cap cavity depths, respectively.

$$\delta = \frac{1}{\beta} = \sqrt{\frac{2\nu_{air}}{\omega_0}} \quad (2)$$

$$c_{comb} = 4ndL_o\mu_{air}\beta \times \frac{\sin 2\beta g + \sinh 2\beta g}{\cosh 2\beta g - \cos 2\beta g} \quad (3)$$

$$c_{cavity} = (4WL + 2nW_cL_c)\mu_{air}\beta \times \left( \frac{\sin 2\beta h_c + \sinh 2\beta h_c}{\cosh 2\beta h_c - \cos 2\beta h_c} + \frac{\sin 2\beta h_s + \sinh 2\beta h_s}{\cosh 2\beta h_s - \cos 2\beta h_s} \right) \quad (4)$$

Since the comb damping coefficient is constant when the resonant structure is determined, the overall air damping of resonators is primarily affected by the depths of the substrate and cap cavities. Specifically,  $c_{comb}$  can be calculated as  $\sim 6.0 \times 10^{-6}$  N·s/m using Eq. (3). Using Eq. (4),  $c_{cavity}$  can be calculated with different substrate and cap cavity depths. In the calculations, the substrate and cap cavity depths are equally assigned. As seen in Fig. 2, the cavity damping coefficient decreases significantly with increasing substrate and cap cavity depths when the cavity depth is less than  $\sim 10$   $\mu\text{m}$ . However, the cavity damping coefficient no longer varies with the substrate and cap cavity depths when the cavity depth is above  $\sim 10$   $\mu\text{m}$ . As explained with the unconfined fluid regime, <sup>(20)</sup> the resonant structure motion is at the state of an isolated plate when the cavity depth increases to a particular value so that the energy dissipation induced by cavity damping tends to be stable. In addition, the calculated comb and cavity damping coefficients are the same when the cavity depth is about 7  $\mu\text{m}$ , which indicates that cavity damping cannot be neglected in this case. However, the cavity damping coefficient remains only one-third of the comb damping coefficient when the cavity depth is above  $\sim 10$   $\mu\text{m}$ , which indicates that the cavity damping is limited in this case.

### 3.2 Damping simulation

It is worth noting that the damping effect of MEMS resonators in an actual situation is more complex than the 1D simplification of the Navier–Stokes equation. Hence, the finite element

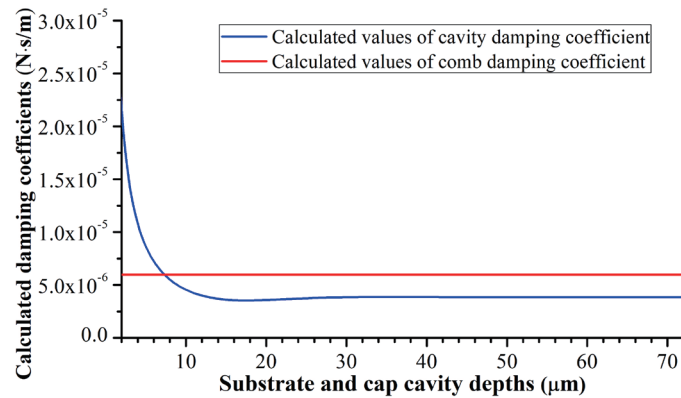


Fig. 2. (Color online) Calculated damping coefficients varied with the substrate and cap cavity depths.

analysis is introduced to determine the effect of cavity depth on air damping. As seen in Fig. 3, the simulation model of a comb pair is adopted to simplify the simulation analysis because of the large number of comb pairs. The simulation model includes the solid structure and air domains; the solid structure domain is composed of the fixed structure (with fixed combs) and movable structure (with movable combs). When the movable structure vibrates back and forth along the x-axis between the fixed combs, the airflow in the air domain produces the drag force. The simulation is performed with the transient analysis in COMSOL Multiphysics, wherein the solid structure and airflow are set as the Si material and laminar flow (with the air pressure of 1 atm), respectively. Also, the airflow is set with the moving mesh. The movable structure is configured to vibrate along the x-axis with an amplitude of 1 μm and a frequency of 37.6 kHz. The laminar flow set is reasonable owing to the vibration amplitude above the mean free pass of the 1-atm air. Then, the overall damping force can be solved by choosing the specific surfaces of the movable structure in Fig. 3. These specific surfaces include two parts: (1) the four sidewalls of movable combs opposite to fixed combs (i.e., comb damping); (2) the top and bottom surfaces of the movable structure opposite to the substrate and cap cavity walls (i.e., cavity damping). The equivalent air-damping coefficient of a comb pair can be obtained by dividing the maximum damping force by the maximum vibration velocity of the movable structure. Thus, the overall air-damping coefficient can be calculated as the product of the equivalent air-damping coefficient of one comb pair and the comb pair number 332.

As shown in Fig. 4, the overall damping coefficient decreases significantly with increases in substrate and cap cavity depths when the cavity depth is less than ~30 μm. In comparison, the overall damping coefficient varies slightly when the cavity depth exceeds ~30 μm. Note that the substrate and cap cavity depths are set with the same value in Fig. 4. In addition, it is found that both the damping force and vibration velocity of the movable structure reach the peak at ~1/2 cycle. Hence, the two typical cases of air velocity field distributions at the 1/2 cycle of simulation models are displayed in Fig. 5. Notably, there is an obvious velocity gradient in the comb clearance and at the top and bottom surfaces of the movable combs, which indicates that the shear resistance resulting from the velocity gradient is the primary air-damping source. As seen

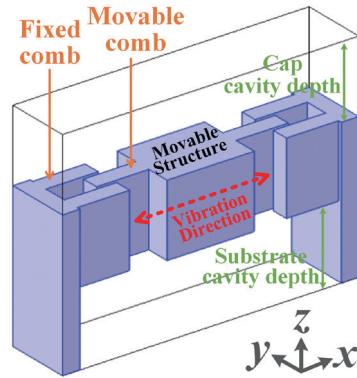


Fig. 3. (Color online) Finite element analysis model of the single comb pair for the MEMS resonator.

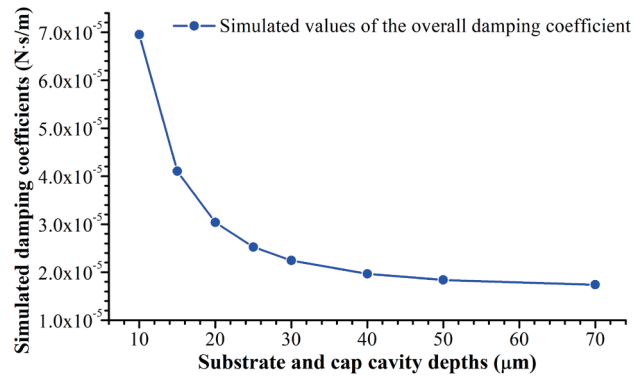


Fig. 4. (Color online) Simulated results of the overall damping coefficient varied with cavity depths.

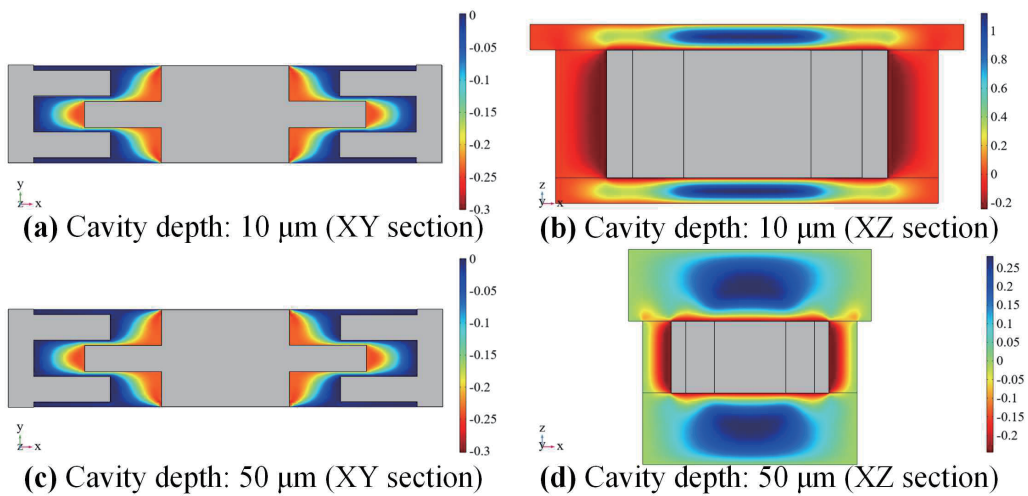


Fig. 5. (Color online) Half-period velocity distributions for the simulation model of the single comb pair.

in Figs. 5(a) and 5(c), the half-period velocity distribution on the  $XY$  section appears similar for cavity depths of 10 and 50  $\mu\text{m}$ . However, in Figs. 5(b) and 5(d), the velocity distribution on the  $XZ$  section for the cavity depth of 10  $\mu\text{m}$  is different from that for the cavity depth of 50  $\mu\text{m}$ . As for the cavity depth of 10  $\mu\text{m}$ , the maximum air velocity induced by cavities is nearly five times greater than that induced by combs, which means that the effect of cavity damping here is more distinct than that of comb damping. The maximum air velocities induced by the comb and cavity are similar for the cavity depth of 50  $\mu\text{m}$ , which implies the weak effect of cavity damping. Therefore, the slide-film damping induced by the substrate and cap cavities holds a non-negligible weight ratio in the overall air-damping effect. In fact, the critical cavity depth affecting the damping performance is  $\sim 30$   $\mu\text{m}$  on the basis of simulation results, which is larger than that ( $\sim 10$   $\mu\text{m}$ ) deduced from the 1D Navier–Stokes equation. Nonetheless, the variation relationship of air damping coefficients with cavity depths is consistent, which offers a fundamental reference for optimizing the design of cavity depths.

## 4. Experiment and Discussion

### 4.1 Device fabrication

As shown in Fig. 6 and Table 2, four typical cases of device cavities are adopted to discuss the actual damping effect of the MEMS resonators. These four cases can be summarized as two types: the bare device in Figs. 6(a) and 6(b) and the wafer-level-packaged devices in Figs. 6(c) and 6(d). Actually, the basic device structures and fabrication processes of wafer-level-packaged devices are consistent with those of the bare device. Firstly, substrate cavities with a certain depth were formed at the bottom of device wafers adopted with Si by KOH etching or DRIE after the first lithography. Then, device wafers were bonded with substrate wafers (e.g., glass or silicon). The device wafer side of bonded wafers was thinned to a certain thickness by KOH

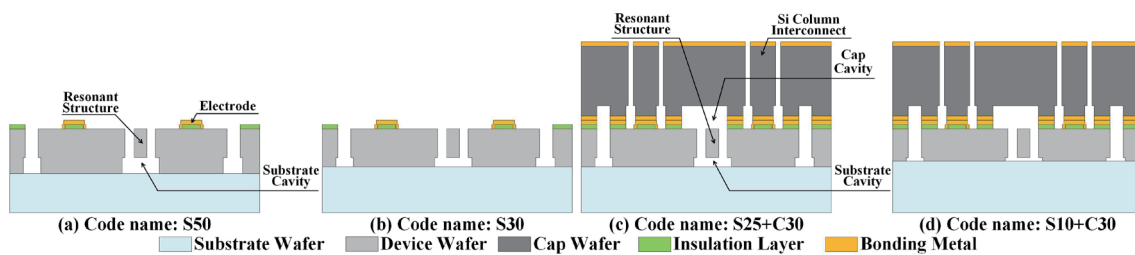


Fig. 6. (Color online) Diagrams of MEMS resonators fabricated with various substrate and cap cavity depths.

Table 2.

Various substrate and cap cavity depths of MEMS resonators fabricated in this work.

Code name	S50 ( $\mu\text{m}$ )	S30 ( $\mu\text{m}$ )	S25 + C30 ( $\mu\text{m}$ )	S10 + C30 ( $\mu\text{m}$ )
Substrate cavity depth	50	30	25	10
Cap cavity depth	N/A	N/A	30	30

etching. After that, an insulation layer was deposited on the bonded device wafers by PECVD and further patterned by RIE after the second lithography to form metal/silicon contact windows. Subsequently, a bonding metal layer (e.g., TiW/Au) was deposited on the bonded device wafers by sputtering and patterned to form electrodes after the third lithography. Afterwards, MEMS resonators were released by DRIE after the fourth lithography. At this stage, the MEMS resonator structures were completed as the bare device in Figs. 6(a) and 6(b).

Note that wafer-level packaging processes for devices are described in detail in our previous work.<sup>(17,18)</sup> Specifically, a bonding metal layer (e.g., Ti/Au) was sputtered on the cap wafers adopted with low-resistivity Si ( $\sim 0.01 \Omega\cdot\text{cm}$ ) and then patterned by wet etching after the fifth lithography. On the basis of the bonding metal patterns, cap cavities with a certain depth were formed on the cap wafers by DRIE at the same time. Then, the cap wafers were bonded with the prepared MEMS resonator wafers by eutectic bonding (e.g., Au-Si bonding). Subsequently, a metal layer (e.g., Ti/Au) was sputtered on the bonded cap wafers and patterned by wet etching after the sixth lithography. Moreover, Si column interconnects used for vertical signal interfaces in packages were formed by DRIE. The packaged structures were completed as the wafer-level packaged devices in Figs. 6(c) and 6(d). The fabricated MEMS resonator chips with comb structures are displayed in Fig. 7.

#### 4.2 Test results and discussion

To compare the damping performance characteristics of fabricated devices at the same air pressure, non-airtight-packaged devices with leakage behavior are selected for the two wafer-level-packaging cases in Figs. 6(c) and 6(d). Every three chips are adopted in the analysis for the four cases in Fig. 6. The air-damping performance of a MEMS resonator can be revealed from the quality factor ( $Q$ -factor,  $Q$ ). Specifically, the smaller  $Q$ -factor acquired from amplitude-frequency characteristics indicates the heavier air-damping effect in devices when resonator structures are the same in tests. Thus, using a network analyzer, S21 tests under atmospheric pressure are carried out for these fabricated devices to obtain their resonant characteristics. As seen in Table 3, the notable difference in  $Q$ -factor between the four cases presents the undeniable air-damping effect from various cavity depths.

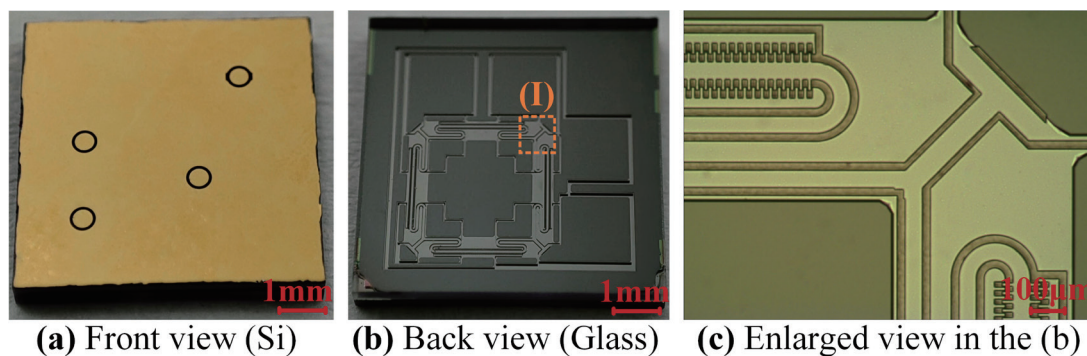


Fig. 7. (Color online) Optical images of a wafer-level-packaged MEMS resonator chip after wafer dicing.

Tab. 3. Measured  $Q$ -factors of MEMS resonators under different substrate and cap cavity depths.

Code name	$Q$ -factor, No.1	$Q$ -factor, No.2	$Q$ -factor, No.3	Mean and standard deviation value
S50	637.2	634.0	631.0	$634.1 \pm 3.1$
S30	538.0	528.4	532.8	$533.1 \pm 4.8$
S25 + C30	356.1	358.0	358.8	$357.6 \pm 1.4$
S10 + C30	228.0	231.0	211.9	$223.7 \pm 10.3$

The MEMS resonator motion can be described with a 1D spring-mass-damping system, which is determined by the equivalent stiffness  $K$ , mass  $M$ , and damping coefficient  $c$ . Also, the  $Q$ -factor and resonant frequency  $f_0$  (or the angular frequency  $\omega_0$ ) of this system can be expressed as Eqs. (5) and (6), respectively. Since the resonant structures are the same, the  $K$  and  $M$  of the mentioned devices are constant. Hence, the actual damping coefficient  $c_{test}$  can be derived from the measured  $Q$ -factors of  $Q_{test}$  using Eq. (5). Actually, the resonance frequency can be acquired from the modal analysis in the finite element simulation. In the modal simulation, the equivalent mass  $M$  of resonators can be obtained as  $\sim 7.994 \times 10^{-8}$  kg using the Rayleigh method. Then, the equivalent stiffness  $K$  can be derived as  $\sim 4.462 \times 10^3$  N/m from Eq. (6). Therefrom, the overall damping coefficient of the fabricated devices can be deduced from the measured  $Q$ -factor values in Table 3. In Fig. 8, the overall damping coefficient values of MEMS resonators, which originate from the theory calculation, simulation, and actual test, are summarized under different substrate and cap cavity depths.

$$Q = \sqrt{KM}/c \Rightarrow c_{test} = \sqrt{KM}/Q_{test} \quad (5)$$

$$\omega_0 = 2\pi f_0 = \sqrt{K/M} \Rightarrow K = (2\pi f_0)^2 \cdot M \quad (6)$$

As seen in Fig. 8, a downward trend of the overall damping coefficient with the decrease in cavity depth can be observed from the simulation and test results. The downward rate of test results is more significant than that of simulation results. However, the calculated values of the overall damping coefficient remain stable. Additionally, there are clear differences in the overall damping coefficients acquired from the theory calculation, simulation, and actual test, which can be illustrated by the following two main reasons.

- (1) Actually in the theory calculation and simulation, note that the long beam elements are only taken into account for the air-damping analysis of combs and cavities. As shown in Fig. 1, the coupled beam structure of the eight folded beams also vibrates in the device resonance mode, which contributes to the new damping interaction with cavity walls. Compared with the theory calculation and simulation, the air damping of folded beams is included in the experimental test.
- (2) For the substrate and cap cavities formed by etching, cavity depths are usually uneven while cavity surfaces are not smooth, which inevitably results in a more severe cavity-damping

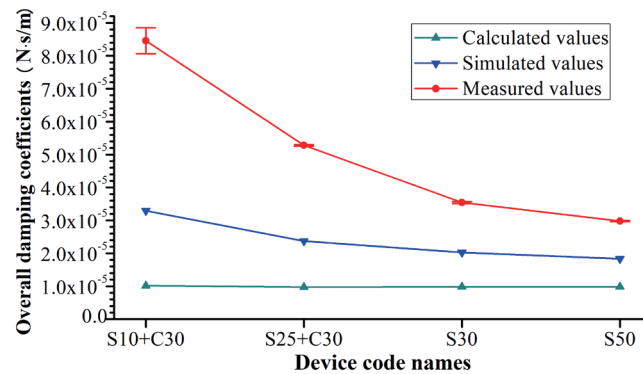


Fig. 8. (Color online) Overall damping coefficients of MEMS resonators from the calculation, simulation, and actual test.

effect than the ideal occasion. In the release process of resonator structures, the side walls of comb structures are not ideally vertical and smooth owing to the over-etching of DRIE, which leads to the more severe effect of comb damping. However, the overall damping coefficients acquired from tests are introduced by all the damping effects in the fabricated devices, e.g., the comb, cavity, coupled beam structure, surface roughness, and size inhomogeneity. Hence, it is reasonable to find that the damping coefficients acquired from the theory calculation and simulation are smaller than those from the actual device test.

Note that the simulation results for the damping coefficient and its variation tendency are more in agreement with the test results than with the theory calculation results. To reduce the cavity-depth damping effect, it is a conservative strategy to choose a relatively large cavity depth by comparing the theory and simulation results. In other words, it will result in a distortion if air damping is only analyzed by theory calculation. For example, the critical cavity depth values of  $\sim 10$  and  $\sim 30$   $\mu\text{m}$  are based on the theory calculation and simulation in Figs. 2 and 4, respectively. If the device cavity design follows the theory value rather than the simulation value, cavity damping will distinctly intensify a resonant system's air-damping effect and deteriorate the resonators'  $Q$ -factors. Consequently, determining the air-damping effect by the combination of theory and simulation analyses is prominent for the optimization design of device damping, especially for the overlooked element of cavity structures in a resonant system dominated by slide-film damping.

## 5. Conclusions

In this paper, we discussed the impact of cavity depth on the 3D wafer-level-packaged MEMS resonators dominated by slide-film damping through theory calculations, simulations, and experimental tests. We found that there is an inverse relationship between the damping coefficient and the cavity depth, while the damping coefficient remains stable for a cavity depth above a certain value. Considering that the simulation result accords more with the test result than with the theoretical prediction, it is essential to choose a relatively large conservative cavity

depth from the combination of theory and simulation analyses to realize high- $Q$ -factor resonators working at low-vacuum or atmospheric pressure. This work can provide the optimization design strategy of slide-film damping caused by cavities for bulk-micro-machined resonators and their wafer-level packaging processes.

### Acknowledgments

This work has been supported by the National Natural Science Foundation of China (Nos. 62241105, 62301226, and 32271997), the Guangzhou Science and Technology Plan Project (No. 2024A04J4759), and the Guangdong Basic and Applied Basic Research Foundation (No. 2020A1515110890).

### References

- 1 M. Bao: Analysis and Design Principles of MEMS Devices (Elsevier, 2005). <https://doi.org/10.1016/B978-0-444-51616-9.X5000-0>
- 2 A. Wang, S. Sahandabadi, T. Harrison, D. Spicer, and M. J. Ahamed: *Microsyst. Technol.* **28** (2022) 2529. <https://doi.org/10.1007/s00542-022-05385-7>
- 3 R. J. Dolleman, D. Davidovikj, S. J. Cartamil-Bueno, H. S. van der Zant, and P. G. Steeneken: *Nano Lett.* **16** (2016) 568. <https://doi.org/10.1021/acs.nanolett.5b04251>
- 4 R. Farrugia, B. Portelli, I. Grech, D. Camilleri, O. Casha, J. Micallef, and E. Gatt: *Microsyst. Technol.* (2019) 1. <https://doi.org/10.1007/s00542-019-04416-0>
- 5 J. Cheng, W.-g. Liu, Q. Chen, N. Xu, Q. Sun, Y. Liu, W. Wang, and H. Xie: *Sens. Actuators, A* **271** (2018) 398. <https://doi.org/10.1016/j.sna.2017.11.043>
- 6 F. Tounsi, B. Mezghani, L. Rufér, and M. Masmoudi: *Archiv. Acoust.* **40** (2015) 527. <https://doi.org/10.1515/aoa-2015-0052>
- 7 T. Aono, A. Kazama, R. Okada, T. Iwasaki, and Y. Isono: *J. Micromech. Microeng.* **28** (2018) 035004. <https://doi.org/10.1088/1361-6439/aaa2d8>
- 8 Anuroop, D. Bansal, P. Kumar, A. Kumar, Khushbu, and K. Rangra: *Microsyst. Technol.* **25** (2019) 3047. <https://doi.org/10.1007/s00542-018-4186-6>
- 9 S. Larsson, P. Johannisson, D. Kolev, F. Ohlsson, S. Nik, J. Liljeholm, T. Ebefors, and C. Rusu: *J. Phys: Conf. Ser.* **1052** (2018) 012100. <https://doi.org/10.1088/1742-6596/1052/1/012100>
- 10 S. J. Bleiker, M. M. Visser Taklo, N. Lietaer, A. Vogl, T. Bakke, and F. Niklaus: *Micromach.* **7** (2016) 192. <https://doi.org/10.3390/mi7100192>
- 11 R. Elfrink, M. Renaud, T. Kamel, C. de Nooijer, M. Jambunathan, M. Goedbloed, D. Hohlfeld, S. Matova, V. Pop, and L. Caballero: *J. Micromech. Microeng.* **20** (2010) 104001. <https://doi.org/10.1088/0960-1317/20/10/104001>
- 12 R. Elfrink, V. Pop, D. Hohlfeld, T. Kamel, S. Matova, C. de Nooijer, M. Jambunathan, M. Goedbloed, L. Caballero, and M. Renaud: 2009 IEEE Int. Electron Devices Meeting (IEDM) (2009) 1. <https://doi.org/10.1109/IEDM.2009.5424300>
- 13 S. Wang, F. Han, B. Sun, and H. Li: *Sensors* **17** (2017) 1119. <https://doi.org/10.3390/s17051119>
- 14 R. Farrugia, I. Grech, D. Camilleri, J. Micallef, O. Casha, and E. Gatt: 2019 Symposium on Design, Test, Integration and Packaging of MEMS and MOEMS (DTIP) (2019) 1. <https://doi.org/10.1109/DTIP.2019.8752884>
- 15 C. Cheng, K. Liang, C. Chu, and W. Fang: *J. Micromech. Microeng.* **27** (2016) 015002. <https://doi.org/10.1088/0960-1317/27/1/015002>
- 16 S.-W. Cheng, J.-C. Weng, K.-C. Liang, Y.-C. Sun, and W. Fang: *J. Micromech. Microeng.* **28** (2018) 045005. <https://doi.org/10.1088/1361-6439/aaa99b>
- 17 H. Liang, X. He, and B. Xiong: *IEEE Sens. J.* **22** (2022) 14522. <https://doi.org/10.1109/JSEN.2022.3182475>
- 18 H. Liang, S. Liu, and B. Xiong: *J. Micromech. Microeng.* **29** (2019) 035010. <https://doi.org/10.1088/1361-6439/aafb83>
- 19 Y.-H. Cho, B. M. Kwak, A. P. Pisano, and R. T. Howe: *Sens. Actuators, A* **40** (1994) 31. [https://doi.org/10.1016/0924-4247\(94\)85027-5](https://doi.org/10.1016/0924-4247(94)85027-5)
- 20 A. Siria, A. Drezet, F. Marchi, F. Comin, S. Huant, and J. Chevrier: *Phys. Rev. Lett.* **102** (2009) 254503. <https://doi.org/10.1103/PhysRevLett.102.254503>

